Chapter 2
Atomistic Modelling of Nanoindentation of Multilayered Graphene-Reinforced Nanocomposites

Shaker A. Meguid, Ahmed R. Alian, and M.A.N. Dewapriya

Abstract The force-displacement curves, obtained from a nanoindentation experiment, are generally analysed using continuum contact mechanics models. However, the applicability of these models at the nanoscale is questionable due to several inherited nanoscale phenomena, e.g., discreteness, quantum manifestations, and scale effects. Atomistic simulations such as molecular dynamics could provide better insight into the contact mechanics of nanoscale systems. In this chapter, we present a comprehensive molecular dynamics simulations of the contact behaviour of multilayered graphene-reinforced composite systems. Three aspects of the work were considered. The first was concerned with the force-displacement curves resulting from nanoindentation of a polyethylene matrix reinforced by multilayered graphene sheets. The second is concerned with the associated deformation patterns as well as the atomic adhesion associated with the retraction stage of the indenter. The third is concerned with the reinforcement mechanism and fracture behaviour associated with the increase in the number of graphene sheets and their spatial locations within the composite. The results of our work reveal: (a) strong interlayer interaction of graphene results in higher indentation resistance, (b) indentation resistance of a single-layer graphene-coated polyethylene is about 13-fold of the indentation resistance of pure polyethylene, (c) strong atomic adhesion between the indenter and the graphene prevails at the nanoscale, and (d) the proper choice of interlayer separation is critical in achieving the best performance of multilayered graphene-reinforced nanocomposites.

S.A. Meguid (✉) • A.R. Alian • M.A.N. Dewapriya
Mechanics and Aerospace Design Laboratory, Mechanical and Industrial Engineering, University of Toronto, Toronto, ON, M5S 3G8 Canada
e-mail: meguid@mie.utoronto.ca; arowaey@mie.utoronto.ca; nuwand@mie.utoronto.ca

S.A. Meguid, G.J. Weng (eds.), *Micromechanics and Nanomechanics of Composite Solids*, DOI 10.1007/978-3-319-52794-9_2

2.1 Introduction and Background

Nanoindentation tests have been used for material characterization since the 1970s (Pethicai et al. 1983). Recently, these tests have been extensively improved by developing advanced testing instruments and techniques and improved analysis methods (Oliver and Pharr 1992, 2004; Hay et al. 1999; Li and Bhushan 2002). As a result of these recent advances, nanoindentation has now become a vitally important test in characterizing the mechanical properties of various materials ranging from nanocomposites to biological materials (Paul et al. 2014). The focus of the current work is multilayered graphene-reinforced composites.

Due to their better strength-to-weight ratio and stiffness, longer fatigue life, and other superior electro mechanical properties, multilayered composites have proven to be very effective in numerous industries ranging from automotive to biomedical applications (Sinha Ray and Okamoto 2003; Pavlidou and Papaspyrides 2008; Jang and Zhamu 2008). Recent advances in fabricating nanoscale multilayered systems, such as graphene-based multilayered nanocomposites, are pushing the frontiers of conventional nanocomposites research (Raccichini et al. 2014; Richardson et al. 2015). In developing such advanced nanoscale multilayered systems, a thorough understanding of the mechanical behaviour of these systems is essential. This has prompted extensive experimental and theoretical studies of the nanoscale phenomena associated with reinforcement characteristics, contact stresses, force-displacement response, failure criteria, atomic adhesion, and atomic pileup, which are essential in designing high performance nanocomposite systems.

More importantly, however, using graphene in composite materials provides an excellent opportunity to transfer the superior electromechanical properties of graphene, across multiple length scales, up to the macroscopic level. Devices such as electromechanical resonators have been fabricated using both single and multi-layered graphene nanoribbons (Bunch et al. 2007; Chen et al. 2009, 2013). Novel methods for constructing multilayered assembly of graphene have been developed by several groups (Kong et al. 2009; Shen et al. 2009). Recent advances in synthesis of graphene-based multilayered nanostructures are showing promising applications in electrochemical energy storage (Raccichini et al. 2014), solar cells (Wang et al. 2011), and gas sensors (Ji et al. 2010). Such graphene-based layered materials could also be used for structural applications in automotive and aerospace industries. Latest developments in multilayered nanofilm assembly (Richardson et al. 2015) will further accelerate the commercial scale fabrication of multilayered graphene-based composites. In order to understand the mechanics of nanoscale multilayered systems, nanoindentation tests on multilayered silicate/polymer nanocomposites have been conducted by several groups; see, e.g., Bruzaud and Bourmaud (2007) and Aldousiri et al. (2011).

2.1.1 Experimental Techniques in Nanoindentation

Nanoindentation tests using atomic force microscopy have been widely used to characterize the material properties at the nanoscale (Gibson 2014; Díez-Pascual et al. 2015). A typical nanoindenter is composed of a force actuator and a displacement sensor to apply a pre-programmed load/displacement profile on the test specimen by using a hard tip (usually made out of diamond). The shape of the indenter tip is often a three-sided Berkovich pyramid because geometric self-similarity of this geometry creates a simple relationship between indentation depth and contact area (Fischer-Cripps 2011). Other commonly used geometries are the three-sided Berkovich pyramidal indenter and the four-sided Vickers pyramidal indenter. The load and the displacement data acquired during the test are plotted against each other, and the mechanical properties including the elastic modulus and the hardness are calculated using analytical models, which will be presented in the next section.

In order to estimate the hardness and stiffness of a material using nanoindentation, it is necessary to accurately determine the contact area between the specimen and the indenter. In early days, the contact area had been estimated by examining the induced residual impression using optical microscopy and image analysis. However, as the dimensions of the indenters began to approach the atomic level, determining of the contact area accurately became extremely challenging. This challenge prompted the development of depth-sensing indentation technique in which both the applied load and the resulting penetration depth are continuously recorded during the indentation process (Doerner and Nix 1986).

In their recent review, Paul et al. (2014) identified several key challenges and recent advances in nanoindentation experiments. Minor et al. (2006) demonstrated the importance of achieving high load resolution (in the range of nN) because the experiments carried out at a very small scale have shown that the initial yielding could occur at extremely low loads even below the force resolution limit. Cross et al. (2006) resolved this problem and succeeded in achieving smaller indenter displacements and force resolution in the range of nN by using atomic force microscopy for their nanoindentation experiments. Controlling surface chemistry and morphology of the test specimen is also very critical in determining the surface characteristics of the material at the nanoscale level (Song and Srolovitz 2006). Preparing the surfaces of the sample and the tip and conducting the indentation experiment in ultra-high vacuum is considered to be the best method to overcome this problem. In addition, indenter characterization becomes increasingly difficult at the atomic level. At this scale, not only the indenter radius but also the crystallographic direction of the tip and the structure of the stepped crystal surface could become important (Paul et al. 2014). Tip characterization can be carried out by scanning and transmission electron microscopy; however these techniques cannot be used to determine the full three-dimensional structure at the atomic scale (Egberts et al. 2009).

In fact, nanoindentation tests have been employed to measure the elastic properties and mechanical strength of graphene (Lee et al. 2008). Recently, Zandiatashbar et al. (2014) conducted nanoindentation tests of graphene to investigate

the effect of defects on the stiffness and the strength of graphene. The obtained load-displacement curves indicated that the strength of graphene with oxygen adatom is ∼14% smaller than the strength of pristine graphene. Shokrieh et al. (2013) conducted nanoindentation and nanoscratch tests to investigate the wear resistance of graphene-based polymer nanocomposites. They found that 0.5 wt% of graphene improved the scratch resistance and the hardness of polymer by 83% and 50%, respectively. By employing nanoindentation tests, Das et al. (2009) demonstrated that 0.6 wt% of multilayered graphene significantly enhances the stiffness (∼70%) and hardness (∼50%) of treated polymers. A more recent experimental study (Flores et al. 2016) has demonstrated that the stiffness of graphene-polyethylene nanocomposites obtained from dynamic nanoindentation measurements is higher than those obtained from quasi-static tensile tests. Furthermore, they found that the hardness decreases with the increase in the strain rate. In addition, they employed grid indentation, which is a very useful method to study the spatial distribution of mechanical properties, to characterize the surface distribution of the elastic modulus of graphene-based nanocomposites.

2.1.2 Analytical Modelling of Nanoindentation

In addition to the experimental developments, substantial advance has also been made in both analytical and numerical modelling of nanoindentation. The classical continuum mechanics has limited applicability at the nanoscale due to the discrete nature of matter and quantum manifestations at the nanoscale (Luan and Robbins 2005; Tapasztó et al. 2012). However, the continuum concepts are computationally efficient and provide reasonable insights into the mechanical behaviour of graphene-based systems (Liu et al. 2011; Zhang et al. 2012; Xu et al. 2012; Dewapriya et al. 2013, 2014; Dewapriya and Rajapakse 2014). On the other hand, when it comes to modelling a complex system such as graphene-based nanocomposites, the accuracy of continuum models is questionable, because they do not take into account the structural configurations and the complex surface morphologies of nanoscopic systems, which are quite important in modelling mechanical properties at the atomic scale (Odegard et al. 2002; Haque and Ramasetty 2005; Dewapriya et al. 2015; Dewapriya and Rajapakse 2016).

Continuum contact mechanics models (Oliver and Pharr 1992; Pharr et al. 1992; Oliver and Pharr 2004) and Hertzian theory (Vlassak and Nix 1994) are widely used to analyse the force-displacement curves obtained from nanoindentation tests. The Oliver–Pharr method extended the initial analysis conducted by Sneddon (1965) on the indentation of an elastic half space by a flat cylindrical punch, which provided a simple relationship between load and displacement. Using the Sneddon's analysis, Oliver and Pharr established a simple method to estimate the elastic modulus and the hardness of a given material by using loading/unloading curve and the geometry of the indenter. According to the Oliver–Pharr simplified model, the hardness H was calculated to be

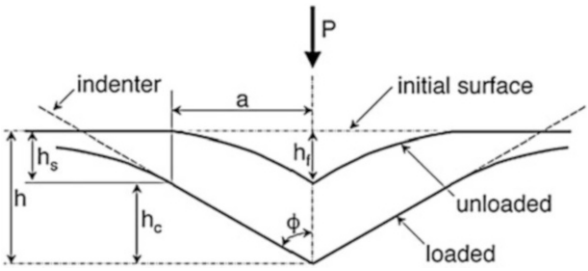

Fig. 2.1 Schematic representation of loaded and unloaded deformations of a specimen during indentation test (Oliver and Pharr 2004)

$$H = \frac{P_{max}}{A} \tag{2.1}$$

where P_{max} is the peak indentation force and A is the contact area between the indenter and the specimen. The value of A depends on the height h_c, which is defined in Fig. 2.1.

The elastic modulus (E) of the specimen can be obtained from the relationship

$$\frac{1}{E_r} = \frac{\left(1-\upsilon^2\right)}{E} + \frac{\left(1-\upsilon_i^2\right)}{E_i} \tag{2.2}$$

where υ and υ_i are the Poisson's ratios of the specimen and the indenter, respectively. E_i is the elastic modulus of the indenter and E_r is the reduced modulus, which takes into account the induced elastic deformations in both the indenter and the specimen. The value of E_r is given as

$$E_r = \frac{\sqrt{\pi}}{2\beta}\frac{S}{\sqrt{A}} \tag{2.3}$$

where S is the initial unloading contact stiffness given by the initial slope of the unloading curve. β is a dimensionless parameter, and its value depends on the geometry of the indenter. Using finite element models, Sakharova et al. (2009) showed that β is 1.034, 1.081, and 1.055 for the axisymmetric conical indenter, the Berkovich pyramidal indenter, and the Vickers pyramidal indenter, respectively.

The model developed by Oliver and Pharr was modified by several researchers in order to overcome its inherited limitations (Oyen and Cook 2003; Tang and Ngan 2003). For example, after several experimental studies demonstrated that the initial portion of the unloading curve is nonlinear (Oliver and Pharr 2004), it was proposed that the unloading curve is better represented by a nonlinear power law in the form

$$P = \alpha\left(h - h_f\right)^m \tag{2.4}$$

where P, h, and h_f are defined in Fig. 2.1; α and m are power law curve-fitting parameters.

However, it is questionable whether the Oliver–Pharr method can be directly applied to nanoindentation of polymers due to their viscoelastic properties (Gibson 2014). The viscoelastic properties could lead to an inaccurate estimate of the

hardness and the stiffness of the considered polymer. As an example, the creep behaviour of polymers could induce a "nose effect" during the unloading stage, leading to an inaccurate estimation of the contact stiffness (Oyen and Cook 2003; Tang and Ngan 2003). Furthermore, McAllister et al. (2012) and Wang et al. (2016) studied the applicability of the Oliver–Pharr method in analysing the load-displacement curves obtained by nanoindentation of polymers. They conducted both experiments and finite element modelling and found that the Oliver–Pharr method can be applied to polymers with a reasonable accuracy. They also revealed that the viscoelastic effects of polymer can be minimized by using high loading/unloading rate and by holding the load for a relatively longer duration. However, the Oliver–Pharr method has several limitations when it is used at the atomic level (McAllister et al. 2012; Yan et al. 2012).

2.1.3 Atomistic Modelling of Nanoindentation

Atomistic modelling and simulation methods such as quantum mechanics (QM) and molecular dynamics (MD) play an important role in investigating the mechanical behaviour of nanoscale material systems. First principle QM calculations have been used to investigate the deformation at the contact region of a silicon (Si) substrate (Pérez et al. 1995). The simulations revealed that the flow of atoms occurs close to the interstitial position inside the Si substrate and extrusion of Si atoms towards the tip, which was made out of aluminium atoms. This extrusion is induced by non-uniform volumetric strain, and it is stabilized by the adhesive interaction with the tip. QM-based models have been used to investigate several mechanical aspects of graphene such as fracture (Khare et al. 2007a; Xu et al. 2012), edge stress and stability (Huang et al. 2009), bending (Kwon et al. 2012), effect of defects (Robertson et al. 2013), and interface mechanics (Xu and Buehler 2010). However, MD simulations are used to investigate the temperature-dependent properties because QM is not able to simulate systems at finite temperatures.

Molecular dynamics simulations have been widely used to study the mechanics of graphene and carbon nanotube (CNT)-based nanocomposites. Meguid and his collaborators used MD simulations to determine the effective elastic properties of a representative volume element that is comprised of CNT nanofillers (Alian et al. 2016; Alian and Meguid 2016; Alian et al. 2015a; b). Xia et al. (2016) conducted course-grained MD simulations of nanoindentation to study the interphase length scale of a polymer. Beyond the interphase length scale, the elastic modulus can be considered to be similar to the elastic modulus of the bulk polymer. They found that the interphase length scale is several tens of nanometres in the case of nanoindentation measurements and also found that this length scale is sensitive to the indenter radii.

Mathew and Sewell (2016) characterized the thermomechanical response of an energetic molecular crystal (i.e. TATB) by conducting MD simulations of nanoindentation. They observed that the elastic part of the force-displacement curve on the

basal plane is accurately predicted by an analytical solution obtained using Hertzian theory of indentation of an anisotropic half space with a rigid, frictionless parabola of revolution (Vlassak and Nix 1994; Willis 1966), whereas non-Hertzian response is demonstrated on the nonbasal planes. Tavazza et al. (2015) investigated the interaction between a diamond tip and nickel (Ni) substrate using MD simulations. They observed a significant amount of Ni atoms transfer to the diamond tip. This material transfer could have a significant impact on the nanoindentation test results. Rocha et al. (2013) used MD simulations to study the indentation behaviour of high-density polyethylene. Their study revealed that increasing the external force results in a decrease in the viscoelastic recovery and that a larger size indenter, under constant external force, generates increased viscoelastic recovery. MD simulations of nanoindentation tests on crystalline cellulose materials (Wu et al. 2013) and synthetic poly-dopamine (Lin et al. 2014) have been conducted to predict the mechanical properties and structure of those advanced materials.

Li et al. (2012) carried out atomistic simulations of the tensile response of thermoset polymer composites reinforced with multilayered graphene. Their results revealed that regardless of the relative orientation of the multilayered graphene and the composite interface, the strength of the composites under uniaxial tension is higher than the corresponding strength for the bulk polymer. Tan et al. (2013) conducted MD simulations to investigate the nanoindentation of circular monolayer graphene. They found that in the small deflection range, the indenter has a near point contact with graphene, and that the point load model is applicable. If the indenter is large, the size effect of the indenter is evident in the large deflection range, and the sphere-load model, which was developed to study spherical indentation of materials (Begley and Mackin 2004; Scott et al. 2004), should be used. Neek-Amal and Peeters (2010) conducted nanoindentation tests on bilayer graphene and found that Young's modulus is 0.8 TPa, which is less than a single-layer sheet. They also found that Young's modulus at 20 K is 14% less than the value at 300 K. A recent MD simulation of tensile behaviour of multilayered graphene shows that the ultimate tensile strength and Young's modulus of multilayered graphene are insensitive to the number of layers (Zhang and Gu 2013).

In this chapter, we present a detailed molecular dynamics simulations of the contact mechanical behaviour of a multilayered graphene-polyethylene composite resulting from numerical nanoindentation tests. Two aspects of the work are considered. First, we conducted molecular dynamics simulations of nanoindentation tests of single- and multilayered graphene. Second, building upon the knowledge obtained from the first part, we investigated the contact mechanical behaviour of multilayered graphene-reinforced polymer composites by conducting numerical nanoindentation tests. This chapter is organized as follows. In Sect. 2.2, the basics of molecular dynamics simulations are explained. Molecular dynamic modelling of nanoindentation of graphene and graphene-reinforced polymer composite is described in detail in Sect. 2.3, and results are also presented in that section. Finally, the concluding remarks are given in Sect. 2.4.

2.2 Basic Concepts of Molecular Dynamics Simulations

The main purpose of MD simulations is to study the time-dependent behaviour of a system by computing the current and the future positions and the velocity of each atom using Newton's equations of motion. This information can be later used to calculate the averaged mechanical properties of the system (Rapaport 1995; van Gunsteren and Berendsen 1990).

The initial position and velocity of each atom of the system must be known at the beginning of the MD simulation. The initial velocities are randomly generated based on the required average temperature of the system. Then, the trajectories of the atoms are determined by solving Newton's equations of motion of the interacting atoms of the system, viz.,

$$\vec{F}_i = m_i \vec{a}_i \tag{2.5}$$

where $\vec{F}_i$, m_i, and $\vec{a}_i$ are the respective acting force, mass, and acceleration of atom i. The interatomic forces are the gradient of the total potential energy V of the system and is given by

$$\vec{F}_i = -\nabla V\left(\vec{r}\right). \tag{2.6}$$

The velocity $\vec{v}_i$ and the acceleration $\vec{a}_i$ of each atom are the first and second derivatives of the displacement vector $\vec{r}_i$, respectively:

$$\vec{v}_i = \frac{d\vec{r}_i}{dt} \tag{2.7}$$

$$\vec{a}_i = \frac{d\vec{v}_i}{dt} \tag{2.8}$$

Using Eqs. (2.5) to (2.8), we can obtain the following differential equation:

$$-\nabla V\left(\vec{r}\right) = m_i \frac{d^2\vec{r}_i}{dt^2}. \tag{2.9}$$

The most popular algorithm to integrate the resulting equations of motion of the system is the Verlet algorithm (Verlet 1967). In this algorithm, Newton's equations of motion are approximated by a Taylor series expansion as a time series, as follows:

$$\mathrm{r}\left(\mathrm{t}+\delta\mathrm{t}\right) = \mathrm{r}\left(\mathrm{t}\right) + \mathrm{v}\left(\mathrm{t}\right)\ \delta\mathrm{t} + \frac{1}{2}\mathrm{a}\left(\mathrm{t}\right)\ \delta\mathrm{t}^2 + \frac{1}{6}\frac{d^3r(t)}{\mathrm{dt}^3}\ \delta\mathrm{t}^3 + \mathrm{O}\left(\delta\mathrm{t}^4\right) \tag{2.10}$$

$$\mathrm{r}\,(\mathrm{t}-\delta\mathrm{t}) = \mathrm{r}\,(\mathrm{t}) - \mathrm{v}\,(\mathrm{t})\ \delta\mathrm{t} + \frac{1}{2}\mathrm{a}\,(\mathrm{t})\ \delta\mathrm{t}^2 - \frac{1}{6}\frac{d^3 r(t)}{\mathrm{dt}^3}\ \delta\mathrm{t}^3 + \mathrm{O}\left(\delta\mathrm{t}^4\right) \tag{2.11}$$

Adding Eqs. (2.10) and (2.11), and moving the r(t − δt) term to the right-hand side, we can obtain

$$r\,(t+\delta t) = 2r(t) - \mathrm{r}\,(\mathrm{t}-\delta\mathrm{t}) + a(t)\ \delta t^2 + O\left(\delta t^4\right) \tag{2.12}$$

This is the general form of the Verlet algorithm for MD, where δt is the time step of the analysis. The accuracy of this approach increases significantly with the decrease in this time step, because it is a function of the fourth order of δt. The value of a(t) is determined from Eq. (2.9), which depends on the location of the atom. Here, we use the positions from the previous and current time steps and acceleration of the current step to predict the trajectory of the atom. The instantaneous velocity $v(t)$ of each atom can be later calculated using the following Taylor series expansion

$$v(t) = \frac{\mathrm{r}\,(\mathrm{t}+\delta\mathrm{t}) - \mathrm{r}\,(\mathrm{t}-\delta\mathrm{t})}{2\delta\mathrm{t}} + O\left(\delta t^3\right) \tag{2.13}$$

The kinetic energy K(t) and the averaged instantaneous temperature T of the system, based on the equipartition theory, can be calculated using the obtained velocities in the following relations:

$$\mathrm{K}\,(\mathrm{t}) = \frac{1}{2}\sum_{\mathrm{i}} \mathrm{m_i}\ (\mathrm{v_i}\,(\mathrm{t}))^2 \tag{2.14}$$

$$\mathrm{T}\,(\mathrm{t}) = \frac{2}{3}\frac{\mathrm{K}\,(\mathrm{t})}{\mathrm{N}\ \mathrm{K_B}} \tag{2.15}$$

where $\mathrm{K_B}$ is the Boltzmann constant.

The total potential energy of the system can be defined by interatomic potentials or molecular mechanics force fields which describe how the atoms interact with each other (LeSar 2013). The selected interatomic potential or force field for the system under investigation must be very accurate for the quantum mechanical processes and to yield reliable results. These potentials and force fields have been developed by several researchers based on quantum mechanics calculations and then validated by comparing their results with experimental tests (Brenner 2000; LeSar 2013). The general expression for the total atomistic potential energy of the system can be written as a many-body expansion that depends on the position of one, two, three, or more atoms at a time (LeSar 2013), such that

$$V\left(\vec{r}_1, \vec{r}_2, \ldots, \vec{r}_N\right) = \sum_{i}^{N} V_1\left(\vec{r}_i\right) + \sum_{i,j}^{N} V_2\left(\vec{r}_i, \vec{r}_j\right) + \sum_{i,j,k}^{N} V_3\left(\vec{r}_i, \vec{r}_j, \vec{r}_{ik}\right) + \ldots \tag{2.16}$$

where V_1 is the one-body term (energy of the isolated atom i due to an external force field such as the electrostatic force), V_2 is the two-body term (pair-wise interactions of the atoms i and j such as Lennard-Jones potential (Jones 1924)), V_3 is the three-body term (three-body interactions and usually called many-body interactions such as Tersoff and Brenner potentials), N is the number of atoms in the system, and $\vec{r}_i$ is the position vector of atom i (Tersoff 1988; Brenner 1990). In this work, we used an inter atomic many-body potential for hydrocarbons called the Adaptive Intermolecular Reactive Empirical Bond Order (AIREBO) potential (Stuart et al. 2000).

The AIREBO potential consists of three sub-potentials, which are Lennard-Jones potential, the torsional potential, and the reactive empirical bond order (REBO) potential. Lennard-Jones potential incorporates the van der Waals forces, and the torsional potential includes the energy due to torsional interactions between atoms. The REBO potential (Brenner 1990) evaluates energy stored in atomic bonds; the energy stored in a bond between atom i and atom j can be expressed as

$$E_{ij}^{REBO} = f\left(r_{ij}\right)\left[V_{ij}^{R} + b_{ij}V_{ij}^{A}\right] \tag{2.17}$$

where V_{ij}^{R} and V_{ij}^{A} are the repulsive and the attractive potentials, respectively; b_{ij} is the bond order term, which modifies V_{ij}^{A} according to the local bonding environment; r_{ij} is the distance between the atoms i and j; $f(r_{ij})$ is the cut-off function, which limits the interatomic interactions to the nearest neighbours. The cut-off function in REBO potential (Brenner 1990), given in Eq. (2.18), limits the interatomic interactions to the nearest neighbours, such that

$$f\left(r_{ij}\right) = \begin{cases} 1, & r_{ij} < R^{(1)} \\ 1 + \cos\left[\frac{\pi\left(r_{ij} - R^{(1)}\right)}{\left(R^{(2)} - R^{(1)}\right)}\right], & R^{(1)} < r_{ij} < R^{(2)} \\ 0, & R^{(2)} < r_{ij} \end{cases} \tag{2.18}$$

where $R^{(1)}$ and $R^{(2)}$ are the cut-off radii, which are determined to be 1.7 and 2 Å, respectively. The values of cut-off radii are defined based on the first and the second nearest neighbouring distances of the relevant hydrocarbon. The cut-off function, however, causes non-physical strain hardening in carbon nanostructures (Shenderova et al. 2000). Therefore, the modified cut-off radii, ranging from 1.9 to 2.2 Å, have been used to eliminate this non-physical strain hardening (Jhon et al. 2014; Zhang et al. 2012; Zhao and Aluru 2010). High strains and fracture of carbon–carbon bonds are possible during nanoindentation test simulations. Therefore, we investigated the influence of the cut-off function on the nanoindentation test results by using a truncated cut-off function $f_t(r_{ij})$, given in Eq. (2.19) (Dewapriya 2012; Dilrukshi et al. 2015).

$$f_t\left(r_{ij}\right) = \begin{cases} 1, & r_{ij} < R \\ 0, & r_{ij} > R \end{cases} \tag{2.19}$$

where the value of R is 2 Å. Similar cut-off functions have been used by Zhang et al. (2012) and Cao and Qu (2013) to simulate the fracture of graphene.

All MD simulations are being conducted under specified conditions. These ensembles are characterized by fixed values of the following thermodynamic variables: potential energy, temperature, pressure, volume, and total number of particles. The most commonly used ensembles in MD simulations are:

- Micro-canonical ensemble: constant number of atoms, volume, and energy (NVE)
- Isothermal-isobaric ensemble: constant number of atoms, temperature, and pressure (NTP)
- Canonical ensemble: constant number of atoms, temperature, and volume (NVT)

There is a common sequence that can be followed to build an MD model and perform a successful simulation. The first step is to build the initial structure of the system using the appropriate software such as Nanoengineer, Materials Studio, Packmol, amongst others. The second step is to optimize this initial structure by changing the location of its atoms relative to each other to reduce the total potential energy of the system and also to release the existing residual stresses. The third step is to assign an initial velocity to each atom based on the targeted average temperature of the system. The fourth step is to equilibrate the minimized structure to obtain the system at targeted initial conditions (pressure, volume, temperature). The final step is to conduct the required analysis and measure the system properties of interest.

2.3 Molecular Dynamics Simulation of Graphene-Reinforced Nanocomposites

The main goal of this study is to determine the reinforcement effect of graphene sheets on nanocomposites. In order to understand the reinforcing mechanism of such composites, MD simulations of the numerical nanoindentation test of pure polymer and both single and multilayered graphene structures were conducted. Consequently, numerical nanoindentation tests of multilayered graphene-reinforced systems with different configurations followed. The results of the MD simulations for all the systems considered are presented and compared in order to give insight into the behaviour of these materials at the nanoscale. All MD simulations were performed with large-scale atomic/molecular massively parallel simulator (LAMMPS; Plimpton 1995) using the adaptive intermolecular reactive bond order (AIREBO) potential (Stuart et al. 2000).

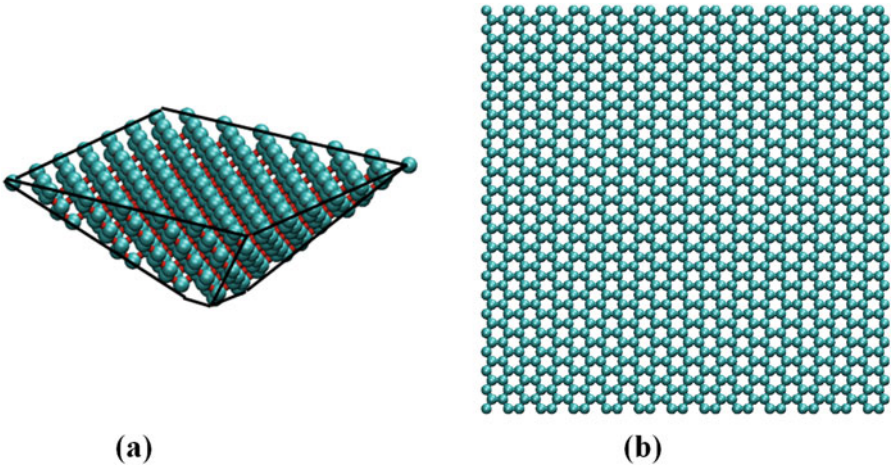

Fig. 2.2 Preliminary system used for the nanoindentation simulations. (**a**) The pyramid-shaped diamond indenter with dimensions of 24 × 24 × 10 Å and (**b**) the graphene sheet with dimensions of 50 × 50 Å

2.3.1 Indentation of a Single Layer of Graphene

We used a pyramid-type diamond indenter (Vickers indenter) for the nanoindentation simulations. Figure 2.2 shows the diamond indenter and the graphene sheet used for the study. The base of the indenter selected was 24 × 24 Å with a thickness of 10 Å. The indenter tip consists of 9 carbon atoms (3 × 3 atoms). In a graphene sheet, carbon atoms are arranged in a honeycomb lattice, where the carbon–carbon bond length is assumed to be 1.396 Å (Stuart et al. 2000). The dimensions of the graphene target selected were 50 × 50 Å, and it has 1070 carbon atoms. The MD simulations were conducted at a temperature of 300 K with a time step of 0.5 fs. The energy of the system (the graphene target and the indenter) was firstly minimized using the Conjugate Gradient algorithm. The system was considered to be optimized once the change in the total potential energy between subsequent steps is less than 1.0×10^{-10} kcal/mol (Alian and Meguid 2017). Then, the minimized system was allowed to reach equilibrium over 50,000 time steps in the constant temperature and volume (NVT) ensemble. Figure 2.3 shows the system reaching equilibrium after some 5 ps.

The initial gap between the indenter tip and the graphene target was selected to be 15 Å as the system reaches its equilibrium. The diamond indenter was brought into contact with the graphene target at a constant speed of 1 Å/ps, and the resisting force on the indenter was calculated at each simulation step and also averaged over an interval of 0.1 ps to reduce the effect of fluctuations on the obtained results. The MD unit cell was equilibrated using the NVT ensemble at 300 K during the indentation process. Four edges of the graphene target were kept fixed during the indentation, and the diamond indenter was considered as a rigid body (i.e. constant

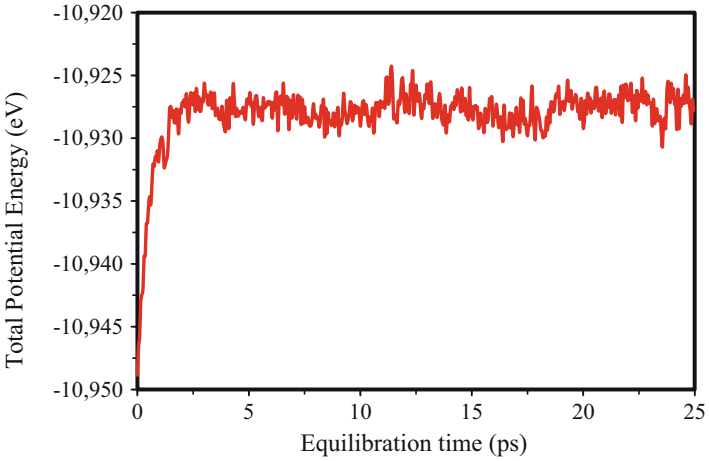

Fig. 2.3 Variation in potential energy of the simulated system with the equilibration time

speed in z direction and zero speed in x and y directions). The indentation process continued until the graphene sheet was fractured to establish the upper bound of indentation depth and the associated indenter force. Figure 2.4 demonstrates the corresponding deformation and the fracture behaviour of the graphene sheet during the indentation process. The figure shows the severe deformation of the graphene sheet upon fracture revealing its extraordinary out-of-plane flexibility. Interestingly, however, even at fracture, several carbon chains hold the two fractured entities of the graphene together, as shown in Fig. 2.4d. Similar phenomenon had been observed in experiments (Chuvilin et al. 2009; Jin et al. 2009) as well as in MD/QM simulation studies (Hobi et al. 2010). These linear carbon chains represent connected dimers composed of two coordinated carbon atoms. Hobi et al. (2010) revealed that in the absence of such dimers, full rupture of graphene will take place.

Figure 2.5 shows the change in the indenter force versus the total potential energy of the system with the indentation time. The indenter touches the graphene sheet at 3 ps. Fracture of the graphene target occurs at an indentation depth of 20 Å, and the maximum indenter force is 510 nN. It can be seen in the figure that the indenter experiences a significant resisting force even after the fracture of the graphene target.

In MD simulations of nanoscale systems, selection of the system and boundary condition is very critical in obtaining reliable results (Mattoni et al. 2005; Dewapriya 2012). Therefore, we investigated the influence of the graphene sheet size on the resulting indentation force at a fixed indentation depth by modelling square graphene sheets with various dimensions ranging from 50 to 200 Å. The indentation force at an indentation depth of 17 Å was determined and compared for all cases considered; see Fig. 2.6. It can be clearly seen that the indentation force decreases significantly as the sheet size increases. This is due to the additional stiffness provided by the fixed boundaries in the out-of-plane direction of the graphene sheet during the indentation process.

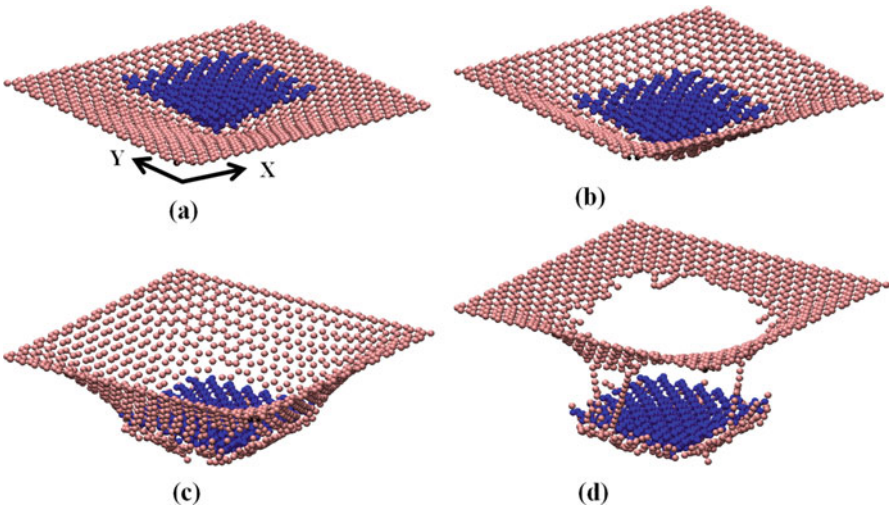

Fig. 2.4 Snapshots of the graphene-indenter system during indentation. The diamond indenter, shown in blue, was moved downwards (along $-z$ direction) at a constant speed of 1 Å/ps. (**a**) and (**b**) show the deformation of the graphene prior to fracture, and (**c**) and (**d**) show the behaviour of graphene after fracture

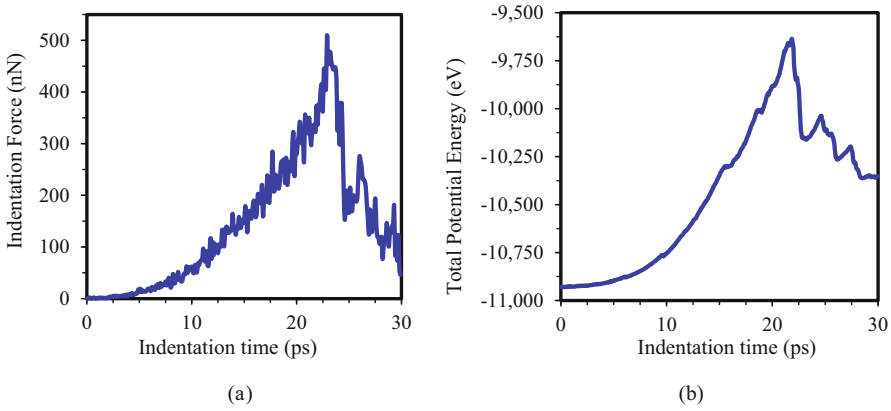

Fig. 2.5 Time variations of (**a**) indentation force versus time and (**b**) system potential energy versus time

The influence of the cut-off function on the indentation force during the MD simulation is investigated in this section. The original and modified cut-off functions are given in Eqs. (2.18) and (2.19), respectively. Even though the original cut-off function introduced non-physical strain hardening of graphene when simulating a tensile test, our study revealed that the influence of a cut-off function on the indentation force is unnoticeable as shown in Fig. 2.7.

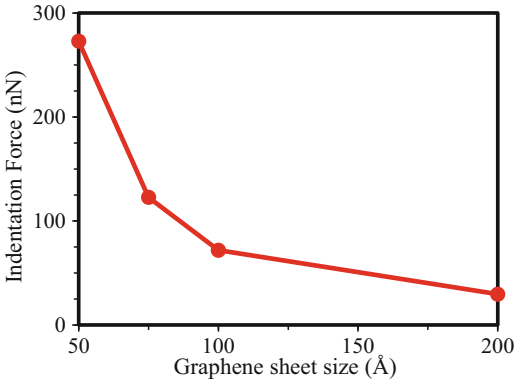

Fig. 2.6 Effect of graphene sheet size upon the resistance to indentation

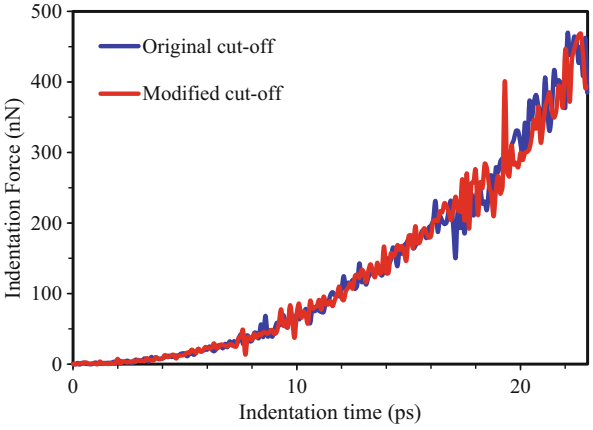

Fig. 2.7 Effect of the interatomic REBO cut-off function on the indentation force of graphene

2.3.2 Indentation of Multilayers of Graphene Sheets

Single-layer graphene sheets tend to agglomerate and form a multilayered system (Li et al. 2008; Shen et al. 2009). The interlayer separation in multilayered graphene is assumed to be 3.4 Å (Lu 1997; Ohta 2006). We performed numerical nanoindentation tests on different multilayered graphene systems consisting of a gradually increasing number of layers up to five sheets. A diamond indenter similar to the one used for the aforementioned single sheet studies (see Fig. 2.2a) but with a longer stem was used for the current simulations. All edges of all multilayered graphene sheets were kept fixed during the indentation stage. The procedures of the MD simulation were similar to that of the single-layer studies, which are explained in Sect. 2.3.1. Figure 2.8 shows indentation of a three-layer graphene sheet for an indentation depth of 30 Å.

Figure 2.9 compares the variation in indentation force with the indentation depth for a different number of layers up to an indentation depth of 20 Å. The figure also shows the best fit polynomial for a single-layer graphene, where the force-depth

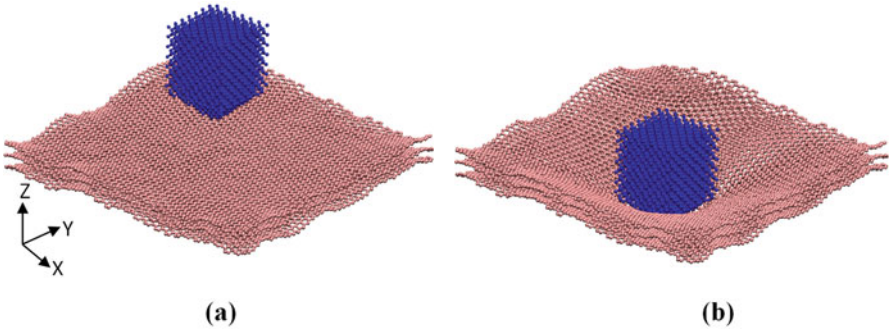

Fig. 2.8 Nanoindentation of a three-layered graphene sheet (**a**) prior to indentation and (**b**) deformed shape during indentation

Fig. 2.9 Variation of indentation force with indentation depth for multilayered graphene targets

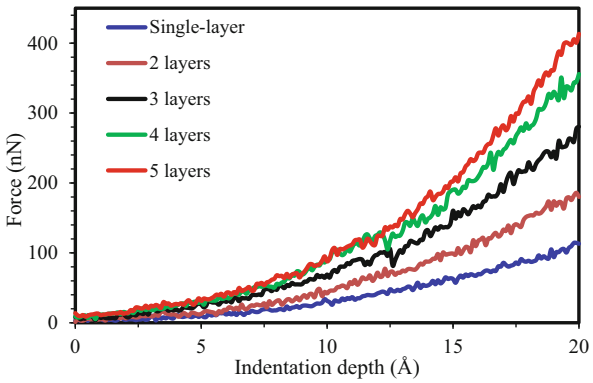

relationship is in the third order as proposed by Lee et al. (2008) and Komaragiri et al. (2005). It can be seen that, at a given indentation depth, the indentation forces of the multilayered graphene cannot be expressed as the linear sum of the indentation force of a single-layer graphene. This is because contact is nonlinear even at the continuum level. In addition, the contact stresses and the resulting contact area are typically unknown a priori.

Figure 2.10 compares the variation of indentation force with the number of graphene sheets at three indentation depths (i.e. 10, 20, and 30 Å). It should be noted that the force is obtained as the average force over 100 time steps in order to obtain more reliable results by reducing the effect of the instantaneous force-time fluctuations. The figure clearly demonstrates an approximately linear relationship between the number of graphene sheets and the indentation force up to five layers. It is also interesting to note that the slope of each curve is different indicating the complexity of the problem.

For example, during the nanoindentation of the five-layered graphene system, all graphene sheets begin to experience some form of fracture around an indentation depth of 27 Å. Figure 2.11a shows the variation in the indentation force during

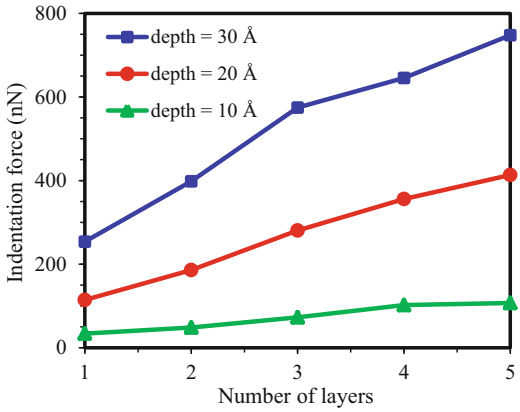

Fig. 2.10 Variation of the maximum indentation force with the number of graphene sheets of a multilayered system at different indentation depths

the indentation process, at $t = 0$, when the indenter is in contact with the top graphene layer. It can be seen in that figure that the indenter experiences a noticeable indentation force even before it touches the top uppermost layer. This force is generated by the repulsive van der Waals interaction forces. Figure 2.11b–g demonstrate the interaction between graphene and indenter at the times shown in Fig. 2.11a. It can be seen in Fig. 2.11c, d that the atoms in contact with the indenter experience highly concentrated deformation. The fracture of the multilayered graphene sheets starts at a depth of 26.5 Å as shown in Fig. 2.11e. Figure 2.11f shows that three graphene sheets are fractured at a depth of 30 Å. After reaching a depth of 30 Å, the indenter was retracted with the same velocity. Figure 2.11g–i show the interaction between the multilayered graphene targets and the indenter during the retraction stage. It can be seen from these figures that there is a significant adhesion between the fractured graphene sheets and the indenter. Fracture of graphene sheet leads to the generation of carbon atoms with dangling bonds which have very high cohesion with the indenter (Alian et al. 2017).

In the following sections, we investigate the mechanical behaviour of polyethylene with and without the use of multilayered reinforcing graphene sheets.

2.3.3 Indentation of Polyethylene

In this section, we will investigate the response of a pure polymer to nanoindentation tests using MD simulations. The results obtained from this analysis will be used as a reference for comparisons with graphene-reinforced polymer nanocomposites. To model the surrounding matrix, a polyethylene (PE) polymer was selected. The unit cell used for the MD simulations consists of 952 PE chains, in which each chain was formed by 10 C_2H_4 units. Planar dimensions (x and y) of the PE block are 100×100 Å and thickness is 50 Å; the density of PE is 0.9 g/cm^3. Periodic boundary conditions were applied along x and y directions. In addition, an invisible surface

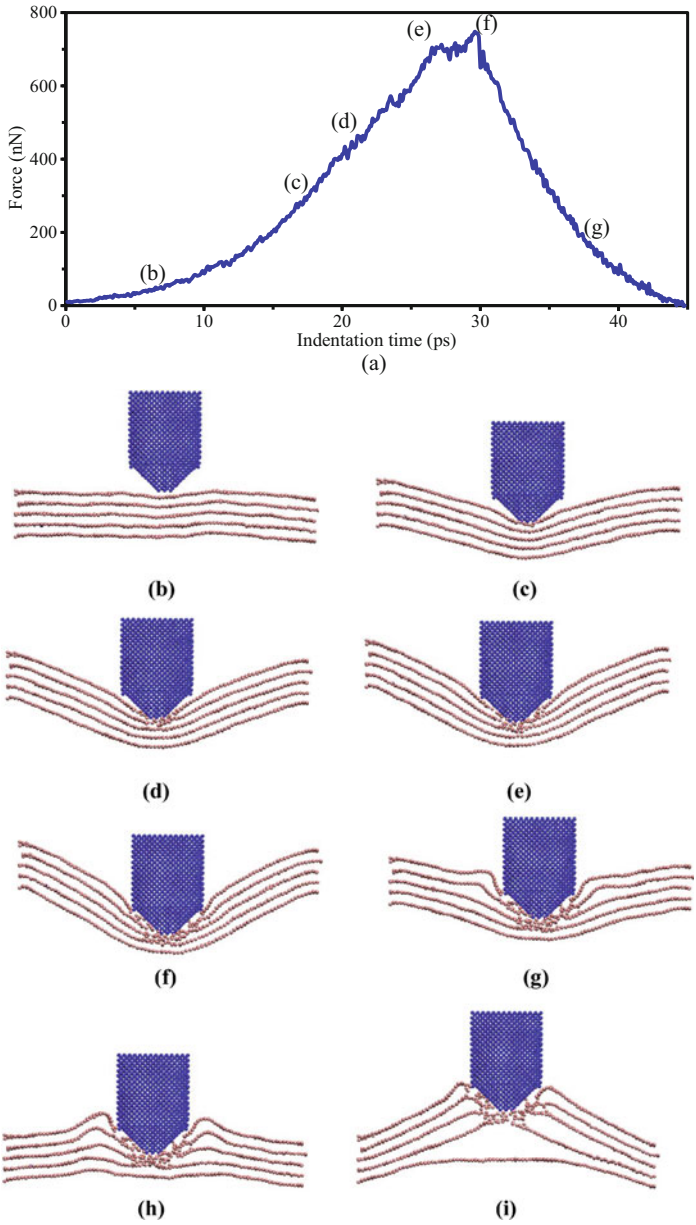

Fig. 2.11 Nanoindentation of five-layered graphene targets: (**a**) Variation in indentation force with time during the test. (**b**)–(**g**) Interaction between graphene and indenter at times indicated as (**b**)–(**g**) on Fig. 2.11a. Figures (**g**)–(**i**) depict behaviour of the system during retraction stage. In Figs. 2.11b–i, a cross section cut through the centre of the indenter was taken in order to demonstrate the position of the indenter and deformation of the different graphene layers

was created just above the PE block to repel any polymer chains from escaping the top polymer surface, while a layer of thickness 3 Å at the bottom of the PE block was kept fixed. The diamond indenter used in the previous sections was used here as well to perform nanoindentation. The procedures of the MD simulation of the indentation test were similar to that of the multilayered graphene system studies, which is explained in Sect. 2.3.2.

Figure 2.12a shows the variation in indentation force during the numerical nanoindentation test, while Fig. 2.12b–d demonstrate the behaviour of the system at different times during the indentation process. Indentation time was measured from the instance where the indenter touches the top of the equilibrated polyethylene system. It can be seen clearly in Fig. 2.12a that the indentation force rapidly increases during the first 12 ps of the indentation stage. After this initial duration, the indentation force increased slightly before reaching its maximum value at a depth of 30 Å. The recorded maximum indentation force in the case of pure polyethylene was 24.5 nN, which represent 10% of the maximum indentation force of a single-layer graphene at the same indentation depth. It can also be seen in Fig. 2.12a that the indentation force does not decrease immediately after the start of the retraction of the indenter at 30 ps. This phenomenon is attributed to the recovery of the polyethylene chains to their original positions and thus maintains the resisting force. However, the polyethylene chains cannot fully return to their original positions at the rate of indenter retraction. In other words, density of polyethylene around the indenter decreases significantly, which eventually leads to a sudden drop in the indentation force at 32 ps.

In the ensuing section, we investigate the contact behaviour of polyethylene matrix reinforced by a single-layer of graphene.

2.3.4 Single-Layer Graphene-Reinforced Polyethylene

In this section, we investigate the reinforcement effect resulting from adding a single-layer of a graphene sheet on the top of the polyethylene used in Sect. 2.3.3. The difference between the composite and the pure polymer will be presented and discussed thoroughly to determine the improvement in the mechanical properties and performance. Figure 2.13 shows a graphene-reinforced polyethylene system. The equilibrium separation distance between the graphene sheet and the polymer matrix is around 3 Å, which was maintained by the repulsive forces between the graphene sheet and the polyethylene atoms in contact with the sheet. Periodic boundary conditions were applied along the x and the y directions of the system, while the graphene sheet was allowed to stand freely on the polymer block.

Figure 2.14 compares the indentation force vs depth relation of a graphene-reinforced polymer composite with the response of a single-layer graphene and that of pure polyethylene. The maximum indentation force for the graphene and the polyethylene are 254 and 24.5 nN, respectively. When these two materials were put together, the maximum indentation force of the combined system becomes

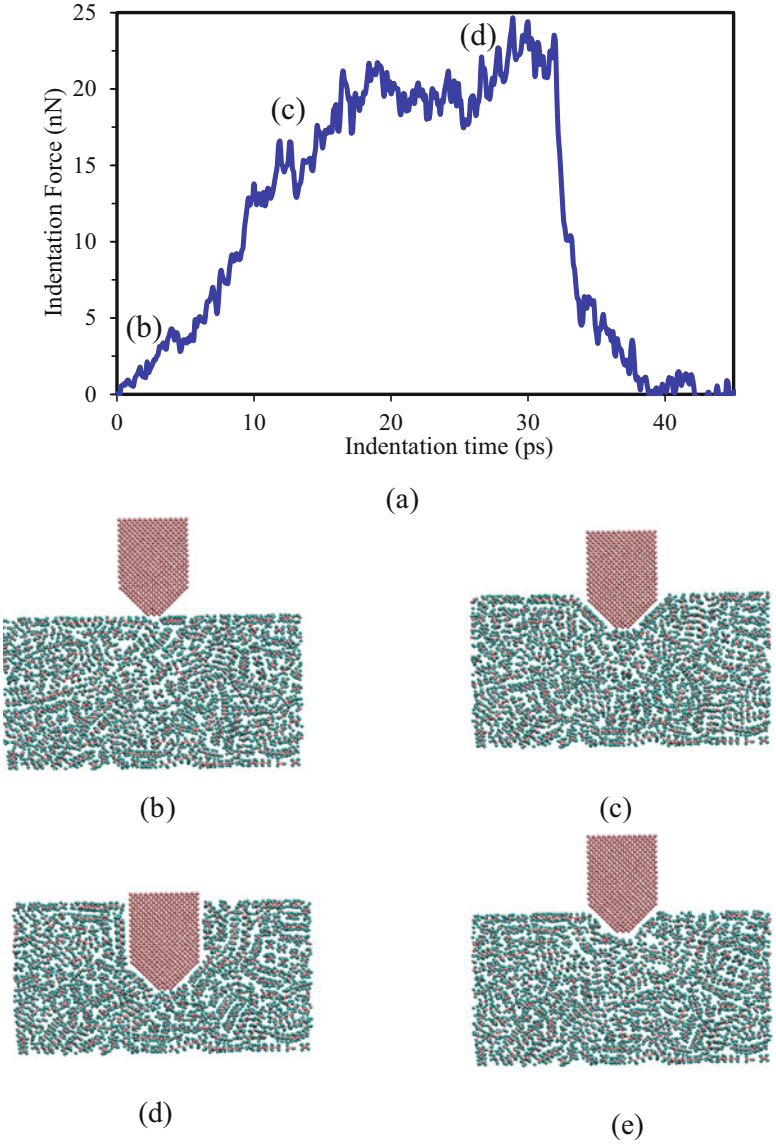

Fig. 2.12 Nanoindentation of polyethylene: (**a**) Variation of force during indentation and retraction of polyethylene matrix. (**b**)–(**e**) Four stages during nanoindentation of polyethylene. A section going through the centre of the indenter was shown in order to demonstrate the position of the indenter and the relative deformation of polyethylene block. (**b**)–(**d**) demonstrate the deformation of polyethylene at times indicated as (**b**)–(**d**) on (**a**)

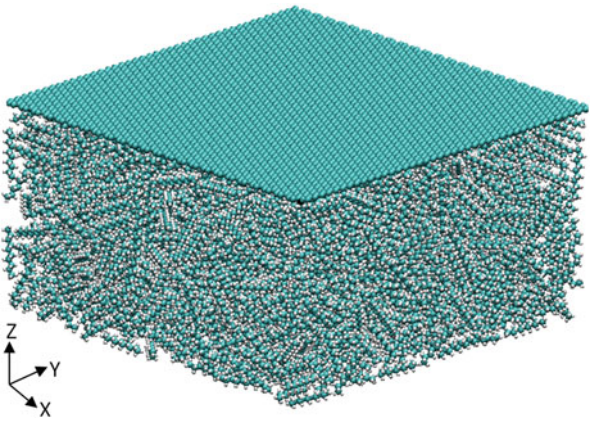

Fig. 2.13 A single-layer graphene-reinforced polyethylene system, which has 67,985 atoms. Dimensions of the polyethylene block are 100 × 100 × 50 Å

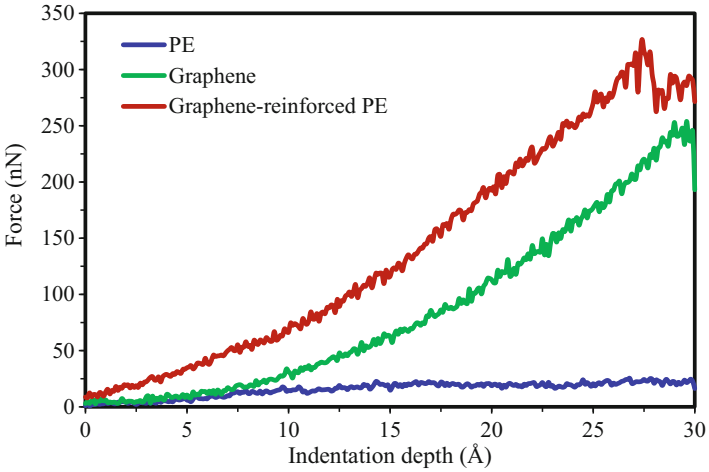

Fig. 2.14 Force-Indentation response for graphene-reinforced polyethylene together with the individual responses of graphene and polyethylene separately

327 nN, which is 13-fold increase in the maximum indentation force of pure polyethylene. In fact, and more remarkably, the indentation resistance of graphene has also increased by 29%. It can be seen in Fig. 2.14 that the graphene-reinforced polyethylene is much stiffer than the combined individual stiffness of graphene and polyethylene. The polyethylene matrix resists the deformation of the graphene sheet, and the graphene sheet is able to distribute the concentrated force exerted by the indenter through a considerably larger area. As a consequence of these two interacting effects, both the graphene and the polyethylene deforms much less than their individual responses to the indentation force, which results in a higher effective stiffness.

2.3.5 *Graphene-Reinforced Multilayered Polyethylene Composites*

Five systems representing PE matrix reinforced with increasing number of graphene sheets that form multilayered structures were considered here. The difference between the response of these systems and the pure polymer to numerical nanoindentation tests will be presented and discussed to determine the improvement in the material performance and also to help designing new nanocomposites with optimized properties. The number of graphene sheets and hence the thickness of the graphene/PE layers range from zero (to represent pure polymer of a thickness of 50 Å) to five layers (to represent a PE layer of 10 Å).

Selecting the system size and boundary conditions properly is very crucial in obtaining accurate and reliable results at a reasonable computational cost. Accordingly, performing MD simulations of large graphene-reinforced polyethylene systems could be computationally very expensive. In order to reduce this burden, we investigated the ability of using smaller structures to model multilayered graphene-reinforced polymer composites. For this purpose, several systems of different sizes were considered to determine the effect of the system size on the obtained properties (i.e. boundary effects). Figure 2.15a–c show the deformation of a multilayered graphene-reinforced polyethylene system during nanoindentation, where the size of the graphene sheets is 50 × 50 Å (designated case A); thickness of individual polyethylene layers is 10 Å, and the system consists of five such layers. Periodic boundary conditions were applied along x and y directions. Indenting/retracting speed of the indenter were 1 Å/ps. It can be seen in Fig. 2.15b that the entire system underwent severe deformation during the indentation process.

The indentation test of a larger system with planar dimensions of 100 × 100 Å (designated case B) was also simulated. Figures 2.15d, e depict snapshots of the larger system before the start of the indentation process at the maximum indentation depth, and after retracting the indenter, respectively. It can be seen in Fig. 2.15e that the boundaries of case A are not severely deformed, and the deformation is mostly localized around the indenter. It is also noticed that the graphene sheet, which was in contact with the indenter, was partially fractured in case B, however the sheet was not fractured in case A. This indicates that even under the same indentation depth, the graphene sheets at the surface of the two system experience totally different levels of deformation. In case A, the entire system (including boundaries) deforms, which can be seen in Fig. 2.15b. However, in case B, the boundaries are slightly deformed as shown in Fig. 2.15e. Therefore, at a given indentation depth, the effective deformation experienced by graphene in case B is higher than that of case A. It can also be seen that there is a significant migration of the polymer chains due to the indentation, which can be clearly seen in Fig. 2.15e. But then, substantial amount of individual polymer chains has come back closer to their original positions during the retraction stage. This polymer migration phenomenon results in a relatively lower density of polyethylene below the indenter. Figure 2.15f demonstrates a significant cohesion between the indenter and the adjacent

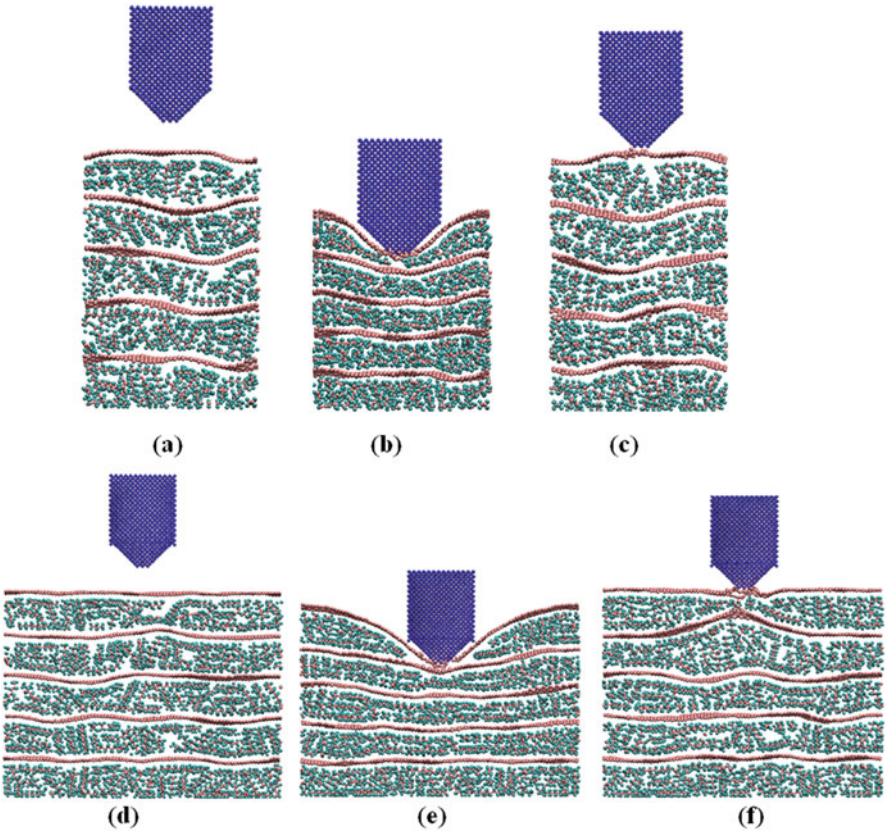

Fig. 2.15 Deformation of multilayered Graphene-PE systems (Cases A and B) considered during nanoindentation. (**a**)–(**c**) depict case A of indentation of 50 × 50 Å, and (**d**)–(**e**) depict case B of indentation of 100 × 100 Å system with five layers

graphene layer and also between indenter and polymer chains in the multilayered system during the retraction stage. One reason for this cohesion is that the graphene sheet has been partially broken which lead to the formation of several dangling bonds on the graphene sheet at the fractured region. The dangling bonds want to be stabilized by creating covalent bonds. Therefore, carbon atoms with dangling bonds have strong cohesion with the diamond indenter and polymer chains (Alian et al. 2017).

Figure 2.16 compares the indentation forces for Cases A and B. There is a 10% difference in the maximum indentation forces of the 50 × 50 Å and 100 × 100 Å systems, which are 307 and 341 nN, respectively. The loading curve of the 50 × 50 Å system indicates that the system is slightly stiffer than the other one. This could be due to the fact that the boundary effects are dominant in case A, whereas this effect lessens in Case B. All polymer layers of case A deform and exert a resisting force on the indenter, but the deformation is localized in case B.

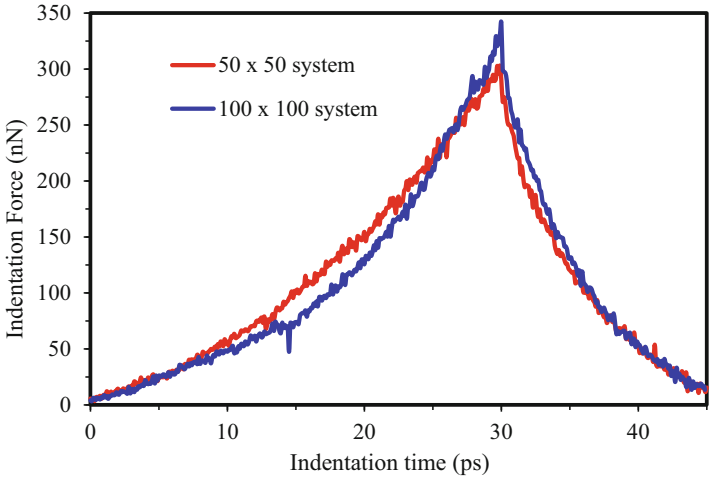

Fig. 2.16 Comparison of indentation force vs time curves of the two five-layered systems shown on Fig. 2.15

Considering the boundary effects, we decided to use a system with planar dimensions of 100 × 100 Å to further investigate the indentation resistance of graphene-reinforced multilayered systems. Figure 2.17 shows the two-, the three-, and the four-layered systems used in the study. Figure 2.18a compares the variation of indentation force with time in all systems, where the indentation was carried out at a speed of 1 ps/Å until the indentation depth of 30 Å is reached. Time is measured from the instant that the indenter touches the uppermost layers of the graphene sheet. The figure reveals that the behaviour of the single, the two, and the three-layered systems is almost identical except that the fracture of a single layer occurs slightly early around an indentation depth of 27 Å; fracture of other systems is not evident. This identical indentation resistance of these layered systems occurred due to the fact that only the uppermost graphene layer is resisting the indenter and that the interior sub-graphene sheets layers do not exert substantial resisting force to the indenter due to the large interlayer separation distance. As an example, Fig. 2.18b shows the deformation of the three-layered system at the maximum indentation depth, and it demonstrates that the second graphene layer does not experience a significant deformation. Therefore, the second layer does not exert any resisting force during the indenter penetration of the first graphene layer. It can be seen that the four-layered system experienced a significant improvement in the performance, which is due to the contribution of the second graphene layer. Surprisingly, however, the performance of the five-layered graphene system is the weakest amongst all the considered systems, even though it was expected to offer greater resistance to indentation due to the higher number of the multilayered graphene sheets. This weakness is attributed to the inability of the 10 Å polyethylene layers to resist the applied load.

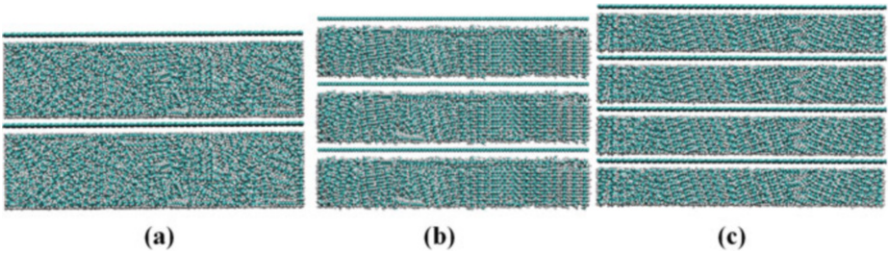

Fig. 2.17 Multilayered graphene-reinforced polyethylene systems. (**a**) The two-, (**b**) the three-, and (**c**) the four-layered systems

Figure 2.18c shows the maximum indentation force of the studied multilayered systems. These results indicate that there is a slight improvement in the maximum resisting force up to three-layered system, where the interlayer spacing is 16.7 Å. When the spacing is reduced from 16.7 to 12.5 Å, there is a 16.5% improvement of the maximum force. However, this improvement completely vanishes when the spacing was further reduced to 10 Å. This result indicates that proper choice of the interlayer separation distance is critically important in achieving the best performance of multilayered graphene-reinforced composites.

2.4 Concluding Remarks

Nanoscale multilayered systems have attracted significant attention in recent research. Graphene has been already proven in its ability to become an exceptional reinforcement for nanocomposites, and graphene-based multilayered systems are believed to be a candidate of the next generation of advanced multifunctional nanocomposites. Recently fabricated graphene-based multilayered nanostructures have demonstrated promising potential for applications in electrochemical energy storage, solar cells, and gas sensors. These multilayered materials could also be used for structural applications in automotive and aerospace industries. Latest developments in multilayered nanofilm assembly will further accelerate the commercial scale fabrication of multilayered graphene-based composites.

In order to design advanced nanoscale multilayered systems with optimized properties, a thorough understanding of the mechanical behaviour of these systems is essential. Even though there is considerable research interest in nanoscale multilayered systems, understanding of their mechanical behaviour is still in its infancy.

Nanoindentation tests using atomic force microscopy have been widely used to characterize the mechanical properties at the nanoscale. The force-displacement data obtained from a nanoindentation test are generally analysed using continuum

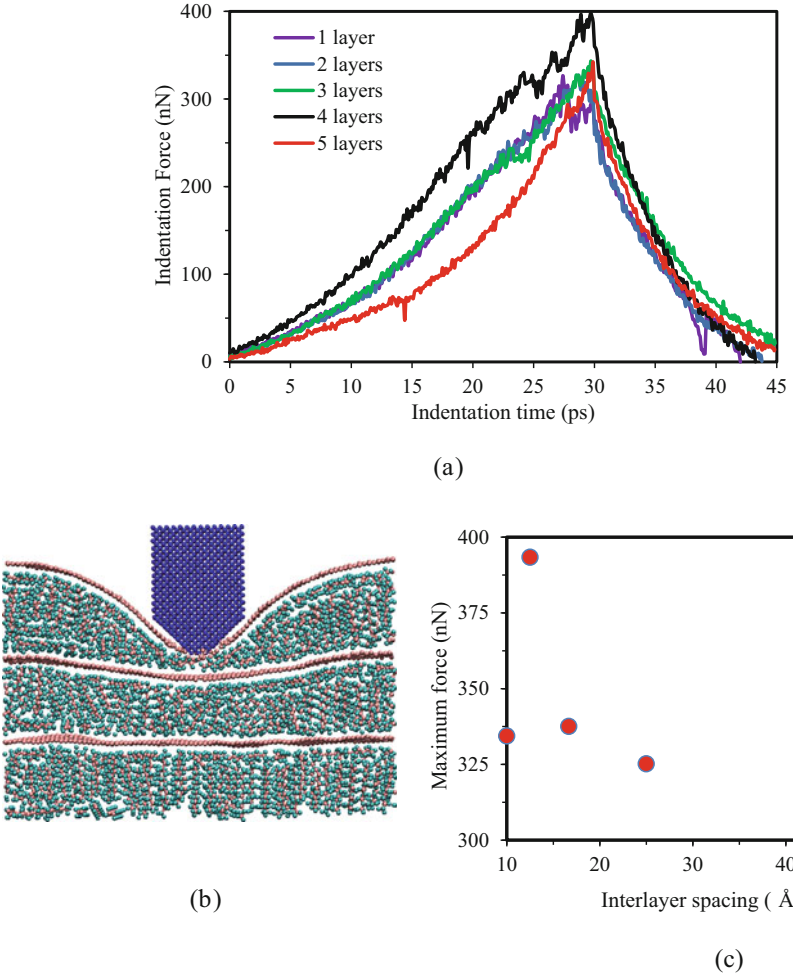

Fig. 2.18 Force-indentation depth of multilayered graphene systems: (**a**) variation of indentation force with time of the multilayered graphene-reinforced systems, (**b**) deformed three-layered system at maximum indentation depth (30 Å), and (**c**) maximum indentation force of the multilayered systems when indented up to 30 Å

contact mechanics models. However, the applicability of continuum models at the atomic level is questionable due to the discrete nature of structures at this scale. Our comprehensive molecular dynamics simulations of the nanoindentation of multilayered graphene-reinforced composites provide significant insight into the force-indentation behaviour of these advanced systems. The results of the molecular dynamics simulations reveal that a strong interlayer interaction has a substantial influence on the material response at the nanoscale.

Furthermore, the observed strong atomic adhesion between the multilayered system and the indenter during indentation could not be studied using existing continuum-based models. Similarly, the atomic adhesion results in a unique deformation pattern that develops during the retraction stage of the indenter. In addition, graphene demonstrated an extraordinary reinforcing influence on the force-indentation predictions. For example, indentation resistance of a single-layer graphene-coated polyethylene is about 13-fold of the indentation resistance of a pure polyethylene target. Significant improvement in the indentation resistance of the multilayered graphene-reinforced system was also observed with the increase of the number of graphene layers. However, proper choice of their spatial locations within the composite is crucial in attaining the greatest resistance to indentation by multilayered graphene-reinforced nanocomposites.

Acknowledgements The authors wish to thank NSERC and the Discovery Accelerator Supplement for their kind support of this research.

References

Aldousiri, B., Dhakal, H.N., Onuh, S., Zhang, Z.Y., Bennett, N.: Nanoindentation behaviour of layered silicate filled spent polyamide-12 nanocomposites. Polym. Test. **30**, 688–692 (2011). doi:10.1016/j.polymertesting.2011.05.008

Alian, A.R., Meguid, S.A.: Molecular dynamics simulations of the effect of waviness and agglomeration of CNTs on interface strength of thermoset nanocomposites. Phys. Chem. Chem. Phys. (2017). doi:10.1039/C6CP07464B

Alian, A.R., Meguid, S.A.: Multiscale modeling of nanoreinforced composites. In: Meguid, S.A. (ed.) Advances in Nanocomposites, pp. 1–39. Springer, Cham (2016)

Alian, A.R., Kundalwal, S.I., Meguid, S.A.: Interfacial and mechanical properties of epoxy nanocomposites using different multiscale modeling schemes. Compos. Struct. **131**, 545–555 (2015a). doi:10.1016/j.compstruct.2015.06.014

Alian, A.R., Kundalwal, S.I., Meguid, S.A.: Multiscale modeling of carbon nanotube epoxy composites. Polymer. **70**, 149–160 (2015b). doi:10.1016/j.polymer.2015.06.004

Alian, A.R., El-Borgi, S., Meguid, S.A.: Multiscale modeling of the effect of waviness and agglomeration of CNTs on the elastic properties of nanocomposites. Comput. Mater. Sci. **117**, 195–204 (2016). doi:10.1016/j.commatsci.2016.01.029

Begley, M.R., Mackin, T.J.: Spherical indentation of freestanding circular thin films in the membrane regime. J. Mech. Phys. Solids. **52**, 2005–2023 (2004). doi:10.1016/j.jmps.2004.03.002

Brenner, D.W.: Empirical potential for hydrocarbons for use in simulating the chemical vapor deposition of diamond films. Phys. Rev. B. **42**, 9458–9471 (1990). doi:10.1103/PhysRevB.42.9458

Brenner, D.W.: The art and science of an analytic potential. Phys. Status Solidi B. **217**, 23–40 (2000). doi:10.1002/(SICI)1521-3951(200001)217:1<23::AID-PSSB23>3.0.CO;2-N

Bruzaud, S., Bourmaud, A.: Thermal degradation and (nano)mechanical behavior of layered silicate reinforced poly(3-hydroxybutyrate-co-3-hydroxyvalerate) nanocomposites. Polym. Test. **26**, 652–659 (2007). doi:10.1016/j.polymertesting.2007.04.001

Bunch, J.S., van der Zande, A.M., Verbridge, S.S., Frank, I.W., Tanenbaum, D.M., Parpia, J.M., Craighead, H.G., McEuen, P.L.: Electromechanical resonators from graphene sheets. Science. **315**, 490–493 (2007). doi:10.1126/science.1136836

Cao, A., Qu, J.: Atomistic simulation study of brittle failure in nanocrystalline graphene under uniaxial tension. Appl. Phys. Lett. **102**, 71902 (2013). doi:10.1063/1.4793088

Chen, C., Rosenblatt, S., Bolotin, K.I., Kalb, W., Kim, P., Kymissis, I., Stormer, H.L., Heinz, T.F., Hone, J.: Performance of monolayer graphene nanomechanical resonators with electrical readout. Nat. Nanotechnol. **4**, 861–867 (2009). doi:10.1038/nnano.2009.267

Chen, C., Lee, S., Deshpande, V.V., Lee, G.-H., Lekas, M., Shepard, K., Hone, J.: Graphene mechanical oscillators with tunable frequency. Nat. Nanotechnol. **8**, 923–927 (2013). doi:10.1038/nnano.2013.232

Chuvilin, A., Meyer, J.C., Algara-Siller, G., Kaiser, U.: From graphene constrictions to single carbon chains. New J. Phys. **11**, 83019 (2009). doi:10.1088/1367-2630/11/8/083019

Cross, G.L.W., Schirmeisen, A., Grütter, P., Dürig, U.T.: Plasticity, healing and shakedown in sharp-asperity nanoindentation. Nat. Mater. **5**, 370–376 (2006). doi:10.1038/nmat1632

Das, B., Eswar Prasad, K., Ramamurty, U., Rao, C.N.R.: Nano-indentation studies on polymer matrix composites reinforced by few-layer graphene. Nanotechnology. **20**, 125705 (2009). doi:10.1088/0957-4484/20/12/125705

Dewapriya, M.A.N.: Molecular Dynamics Study of Effects of Geometric Defects on the Mechanical Properties of Graphene. Department of Mechanical Engineering, University of British Columbia, British Columbia (2012)

Dewapriya, M.A.N., Rajapakse, R.K.N.D.: Molecular dynamics simulations and continuum modeling of temperature and strain rate dependent fracture strength of graphene with vacancy defects. J. Appl. Mech. **81**, 081010 (2014). doi:10.1115/1.4027681

Dewapriya, M.A.N., Rajapakse, R.K.N.D.: Development of a homogenous nonlinear spring model characterizing the interfacial adhesion properties of graphene with surface defects. Compos. Part B: Eng. **98**, 339–349 (2016). doi:10.1016/j.compositesb.2016.04.052

Dewapriya, M.A.N., Srikantha Phani, A., Rajapakse, R.K.N.D.: Influence of temperature and free edges on the mechanical properties of graphene. Model. Simul. Mater. Sci. Eng. **21**, 65017 (2013). doi:10.1088/0965-0393/21/6/065017

Dewapriya, M.A.N., Rajapakse, R.K.N.D., Phani, A.S.: Atomistic and continuum modelling of temperature-dependent fracture of graphene. Int. J. Fract. **187**, 199–212 (2014). doi:10.1007/s10704-014-9931-y

Dewapriya, M.A.N., Rajapakse, R.K.N.D., Nigam, N.: Influence of hydrogen functionalization on the fracture strength of graphene and the interfacial properties of graphene-polymer nanocomposite. Carbon. **1**, 6991–7000 (2015). doi:10.1103/PhysRevB.37.6991

Díez-Pascual, A.M., Gómez-Fatou, M.A., Ania, F., Flores, A.: Nanoindentation in polymer nanocomposites. Prog. Mater. Sci. **67**, 1–94 (2015). doi:10.1016/j.pmatsci.2014.06.002

Dilrukshi, K.G.S., Dewapriya, M.A.N., Puswewala, U.G.A.: Size dependency and potential field influence on deriving mechanical properties of carbon nanotubes using molecular dynamics. Theor. Appl. Mech. Lett. **5**, 167–172 (2015). doi:10.1016/j.taml.2015.05.005

Doerner, M.F., Nix, W.D.: A method for interpreting the data from depth-sensing indentation instruments. J. Mater. Res. **1**, 601–609 (1986). doi:10.1557/JMR.1986.0601

Egberts, P., Filleter, T., Bennewitz, R.: A kelvin probe force microscopy of charged indentation-induced dislocation structures in KBr. Nanotechnology. **20**, 264005 (2009). doi:10.1088/0957-4484/20/26/264005

Fischer-Cripps, A.C.: Nanoindentation, Mechanical Engineering Series, 3rd edn. Springer, New York, NY (2011)

Flores, A., Ania, F., Salavagione, H.J., Ellis, G., Saurel, D., Gómez-Fatou, M.A.: Local mechanical properties of graphene/polyethylene-based nanocomposites by depth-sensing indentation. Eur. Polym. J. **74**, 120–129 (2016). doi:10.1016/j.eurpolymj.2015.11.016

Gibson, R.F.: A review of recent research on nanoindentation of polymer composites and their constituents. Compos. Sci. Technol. **105**, 51–65 (2014). doi:10.1016/j.compscitech.2014.09.016

Haque, A., Ramasetty, A.: Theoretical study of stress transfer in carbon nanotube reinforced polymer matrix composites. Compos. Struct. **71**, 68–77 (2005). doi:10.1016/j.compstruct.2004.09.029

Hay, J.C., Bolshakov, A., Pharr, G.M.: A critical examination of the fundamental relations used in the analysis of nanoindentation data. J. Mater. Res. **14**, 2296–2305 (1999). doi:10.1557/JMR.1999.0306

Hobi, E., Pontes, R.B., Fazzio, A., da Silva, A.J.R.: Formation of atomic carbon chains from graphene nanoribbons. Phys. Rev. B. **81**, 201406 (2010). doi:10.1103/PhysRevB.81.201406

Huang, B., Liu, M., Su, N., Wu, J., Duan, W., Gu, B., Liu, F.: Quantum manifestations of graphene edge stress and edge instability: A first-principles study. Phys. Rev. Lett. **102**, 166404 (2009). doi:10.1103/PhysRevLett.102.166404

Jang, B.Z., Zhamu, A.: Processing of nanographene platelets (NGPs) and NGP nanocomposites: a review. J. Mater. Sci. **43**, 5092–5101 (2008). doi:10.1007/s10853-008-2755-2

Jhon, Y.I., Jhon, Y.M., Yeom, G.Y., Jhon, M.S.: Orientation dependence of the fracture behavior of graphene. Carbon. **66**, 619–628 (2014). doi:10.1016/j.carbon.2013.09.051

Ji, Q., Honma, I., Paek, S.-M., Akada, M., Hill, J.P., Vinu, A., Ariga, K.: Layer-by-layer films of graphene and ionic liquids for highly selective gas sensing. Angew. Chem. **122**, 9931–9933 (2010). doi:10.1002/ange.201004929

Jin, C., Lan, H., Peng, L., Suenaga, K., Iijima, S.: Deriving carbon atomic chains from graphene. Phys. Rev. Lett. **102**, 205501 (2009). doi:10.1103/PhysRevLett.102.205501

Jones, J.E.: On the determination of molecular fields. II. From the equation of state of a gas. Proc. R. Soc. Math. Phys. Eng. Sci. **106**, 463–477 (1924). doi:10.1098/rspa.1924.0082

Khare, R., Mielke, S.L., Paci, J.T., Zhang, S., Ballarini, R., Schatz, G.C., Belytschko, T.: Coupled quantum mechanical/molecular mechanical modeling of the fracture of defective carbon nanotubes and graphene sheets. Phys. Rev. B. **75**, 75412 (2007a). doi:10.1103/PhysRevB.75.075412

Alian, A.R., Dewapriya, M.A.N., Meguid, S.A.: Molecular dynamics study of the reinforcement effect of graphene in multilayered polymer nanocomposites. Materials and Design, 2017 (Accepted).

Komaragiri, U., Begley, M.R., Simmonds, J.G.: The mechanical response of freestanding circular elastic films under point and pressure loads. J. Appl. Mech. **72**, 203 (2005). doi:10.1115/1.1827246

Kong, B.-S., Geng, J., Jung, H.-T.: Layer-by-layer assembly of graphene and gold nanoparticles by vacuum filtration and spontaneous reduction of gold ions. Chem. Commun. **2009**, 2174 (2009). doi:10.1039/b821920f

Kwon, S., Ko, J.-H., Jeon, K.-J., Kim, Y.-H., Park, J.Y.: Enhanced nanoscale friction on fluorinated graphene. Nano Lett. **12**, 6043–6048 (2012). doi:10.1021/nl204019k

Lee, C., Wei, X., Kysar, J.W., Hone, J.: Measurement of the elastic properties and intrinsic strength of monolayer graphene. Science. **321**, 385–388 (2008). doi:10.1126/science.1157996

LeSar, R.: Introduction to Computational Materials Science: Fundamentals to Applications. Cambridge University Press, Cambridge; NY (2013)

Li, X., Bhushan, B.: A review of nanoindentation continuous stiffness measurement technique and its applications. Mater. Charact. **48**, 11–36 (2002). doi:10.1016/S1044-5803(02)00192-4

Li, D., Müller, M.B., Gilje, S., Kaner, R.B., Wallace, G.G.: Processable aqueous dispersions of graphene nanosheets. Nat. Nanotechnol. **3**, 101–105 (2008). doi:10.1038/nnano.2007.451

Li, C., Browning, A.R., Christensen, S., Strachan, A.: Atomistic simulations on multilayer graphene reinforced epoxy composites. Compos. Part Appl. Sci. Manuf. **43**, 1293–1300 (2012). doi:10.1016/j.compositesa.2012.02.015

Lin, S., Chen, C.-T., Bdikin, I., Ball, V., Grácio, J., Buehler, M.J.: Tuning heterogeneous poly(dopamine) structures and mechanics: in silico covalent cross-linking and thin film nanoindentation. Soft Matter. **10**, 457–464 (2014). doi:10.1039/C3SM51810H

Liu, Y., Xu, Z., Zheng, Q.: The interlayer shear effect on graphene multilayer resonators. J. Mech. Phys. Solids. **59**, 1613–1622 (2011). doi:10.1016/j.jmps.2011.04.014

Lu, J.P.: Elastic properties of carbon nanotubes and nanoropes. Phys. Rev. Lett. **79**, 1297–1300 (1997). doi:10.1103/PhysRevLett.79.1297

Luan, B., Robbins, M.O.: The breakdown of continuum models for mechanical contacts. Nature. **435**, 929–932 (2005). doi:10.1038/nature03700

Mathew, N., Sewell, T.D.: Nanoindentation of the triclinic molecular crystal 1,3,5-triamino-2,4,6-trinitrobenzene: a molecular dynamics study. J. Phys. Chem. C. **120**, 8266–8277 (2016). doi:10.1021/acs.jpcc.6b01103

Mattoni, A., Colombo, L., Cleri, F.: Atomic scale origin of crack resistance in brittle fracture. Phys. Rev. Lett. **95**, 115501 (2005). doi:10.1103/PhysRevLett.95.115501

McAllister, Q.P., Gillespie, J.W., VanLandingham, M.R.: Nonlinear indentation of fibers. J. Mater. Res. **27**, 197–213 (2012). doi:10.1557/jmr.2011.336

Minor, A.M., Syed Asif, S.A., Shan, Z., Stach, E.A., Cyrankowski, E., Wyrobek, T.J., Warren, O.L.: A new view of the onset of plasticity during the nanoindentation of aluminium. Nat. Mater. **5**, 697–702 (2006). doi:10.1038/nmat1714

Neek-Amal, M., Peeters, F.M.: Nanoindentation of a circular sheet of bilayer graphene. Phys. Rev. B. **81**, 235421 (2010). doi:10.1103/PhysRevB.81.235421

Odegard, G.M., Gates, T.S., Nicholson, L.M., Wise, K.E.: Equivalent-continuum modeling of nano-structured materials. Compos. Sci. Technol. **62**, 1869–1880 (2002). doi:10.1016/S0266-3538(02)00113-6

Ohta, T.: Controlling the electronic structure of bilayer graphene. Science. **313**, 951–954 (2006). doi:10.1126/science.1130681

Oliver, W.C., Pharr, G.M.: An improved technique for determining hardness and elastic modulus using load and displacement sensing indentation experiments. J. Mater. Res. **7**, 1564–1583 (1992). doi:10.1557/JMR.1992.1564

Oliver, W.C., Pharr, G.M.: Measurement of hardness and elastic modulus by instrumented indentation: advances in understanding and refinements to methodology. J. Mater. Res. **19**, 3–20 (2004). doi:10.1557/jmr.2004.19.1.3

Oyen, M.L., Cook, R.F.: Load–displacement behavior during sharp indentation of viscous–elastic–plastic materials. J. Mater. Res. **18**, 139–150 (2003). doi:10.1557/JMR.2003.0020

Paul, W., Oliver, D., Grütter, P.: Indentation-formed nanocontacts: an atomic-scale perspective. Phys. Chem. Chem. Phys. **16**, 8201 (2014). doi:10.1039/c3cp54869d

Pavlidou, S., Papaspyrides, C.D.: A review on polymer–layered silicate nanocomposites. Prog. Polym. Sci. **33**, 1119–1198 (2008). doi:10.1016/j.progpolymsci.2008.07.008

Pérez, R., Payne, M.C., Simpson, A.D.: First principles simulations of silicon nanoindentation. Phys. Rev. Lett. **75**, 4748–4751 (1995). doi:10.1103/PhysRevLett.75.4748

Pethicai, J.B., Hutchings, R., Oliver, W.C.: Hardness measurement at penetration depths as small as 20 nm. Philos. Mag. A. **48**, 593–606 (1983). doi:10.1080/01418618308234914

Pharr, G.M., Oliver, W.C., Brotzen, F.R.: On the generality of the relationship among contact stiffness, contact area, and elastic modulus during indentation. J. Mater. Res. **7**, 613–617 (1992). doi:10.1557/JMR.1992.0613

Plimpton, S.: Fast parallel algorithms for short-range molecular dynamics. J. Comput. Phys. **117**, 1–19 (1995). doi:10.1006/jcph.1995.1039

Raccichini, R., Varzi, A., Passerini, S., Scrosati, B.: The role of graphene for electrochemical energy storage. Nat. Mater. **14**, 271–279 (2014). doi:10.1038/nmat4170

Rapaport, D.C.: The Art of Molecular Dynamics Simulation. Cambridge University Press, Cambridge, NY (1995)

Richardson, J.J., Bjornmalm, M., Caruso, F.: Technology-driven layer-by-layer assembly of nanofilms. Science. **348**, 2491–2491 (2015). doi:10.1126/science.aaa2491

Robertson, A.W., Montanari, B., He, K., Kim, J., Allen, C.S., Wu, Y.A., Olivier, J., Neethling, J., Harrison, N., Kirkland, A.I., Warner, J.H.: Dynamics of single Fe atoms in graphene vacancies. Nano Lett. **13**, 1468–1475 (2013). doi:10.1021/nl304495v

Rocha, J.R., Yang, K.Z., Hilbig, T., Brostow, W., Simoes, R.: Polymer indentation with mesoscopic molecular dynamics. J. Mater. Res. **28**, 3043–3052 (2013). doi:10.1557/jmr.2013.307

Sakharova, N.A., Fernandes, J.V., Antunes, J.M., Oliveira, M.C.: Comparison between Berkovich Vickers and conical indentation tests: a three-dimensional numerical simulation study. Int. J. Solids Struct. **46**, 1095–1104 (2009). doi:10.1016/j.ijsolstr.2008.10.032

Scott, O.N., Begley, M.R., Komaragiri, U., Mackin, T.J.: Indentation of freestanding circular elastomer films using spherical indenters. Acta Mater. **52**, 4877–4885 (2004). doi:10.1016/j.actamat.2004.06.043

Shen, J., Hu, Y., Li, C., Qin, C., Shi, M., Ye, M.: Layer-by-layer self-assembly of graphene nanoplatelets. Langmuir. **25**, 6122–6128 (2009). doi:10.1021/la900126g

Shenderova, O.A., Brenner, D.W., Omeltchenko, A., Su, X., Yang, L.H.: Atomistic modeling of the fracture of polycrystalline diamond. Phys. Rev. B. **61**, 3877–3888 (2000). doi:10.1103/PhysRevB.61.3877

Shokrieh, M.M., Hosseinkhani, M.R., Naimi-Jamal, M.R., Tourani, H.: Nanoindentation and nanoscratch investigations on graphene-based nanocomposites. Polym. Test. **32**, 45–51 (2013). doi:10.1016/j.polymertesting.2012.09.001

Sinha Ray, S., Okamoto, M.: Polymer/layered silicate nanocomposites: a review from preparation to processing. Prog. Polym. Sci. **28**, 1539–1641 (2003). doi:10.1016/j.progpolymsci.2003.08.002

Sneddon, I.N.: The relation between load and penetration in the axisymmetric boussinesq problem for a punch of arbitrary profile. Int. J. Eng. Sci. **3**, 47–57 (1965). doi:10.1016/0020-7225(65)90019-4

Song, J., Srolovitz, D.J.: Adhesion effects in material transfer in mechanical contacts. Acta Mater. **54**, 5305–5312 (2006). doi:10.1016/j.actamat.2006.07.011

Stuart, S.J., Tutein, A.B., Harrison, J.A.: A reactive potential for hydrocarbons with intermolecular interactions. J. Chem. Phys. **112**, 6472 (2000). doi:10.1063/1.481208

Tan, X., Wu, J., Zhang, K., Peng, X., Sun, L., Zhong, J.: Nanoindentation models and Young's modulus of monolayer graphene: a molecular dynamics study. Appl. Phys. Lett. **102**, 71908 (2013). doi:10.1063/1.4793191

Tang, B., Ngan, A.H.W.: Accurate measurement of tip–sample contact size during nanoindentation of viscoelastic materials. J. Mater. Res. **18**, 1141–1148 (2003). doi:10.1557/JMR.2003.0156

Tapasztó, L., Dumitrică, T., Kim, S.J., Nemes-Incze, P., Hwang, C., Biró, L.P.: Breakdown of continuum mechanics for nanometre-wavelength rippling of graphene. Nat. Phys. **8**, 739–742 (2012). doi:10.1038/nphys2389

Tavazza, F., Senftle, T.P., Zou, C., Becker, C.A., van Duin, A.C.T.: Molecular dynamics investigation of the effects of tip–substrate interactions during nanoindentation. J. Phys. Chem. C. **119**, 13580–13589 (2015). doi:10.1021/acs.jpcc.5b01275

Tersoff, J.: Empirical interatomic potential for silicon with improved elastic properties. Phys. Rev. B. **38**, 9902–9905 (1988). doi:10.1103/PhysRevB.38.9902

van Gunsteren, W.F., Berendsen, H.J.C.: Computer simulation of molecular dynamics: methodology, applications, and perspectives in chemistry. Angew. Chem., Int. Ed. Eng. **29**, 992–1023 (1990). doi:10.1002/anie.199009921

Verlet, L.: Computer "experiments" on classical fluids. I. Thermodynamical properties of Lennard-Jones molecules. Phys. Rev. **159**, 98–103 (1967). doi:10.1103/PhysRev.159.98

Vlassak, J.J., Nix, W.D.: Measuring the elastic properties of anisotropic materials by means of indentation experiments. J. Mech. Phys. Solids. **42**, 1223–1245 (1994). doi:10.1016/0022-5096(94)90033-7

Wang, Y., Tong, S.W., Xu, X.F., Özyilmaz, B., Loh, K.P.: Interface engineering of layer-by-layer stacked graphene anodes for high-performance organic solar cells. Adv. Mater. **23**, 1514–1518 (2011). doi:10.1002/adma.201003673

Wang, Z., Gu, P., Zhang, H., Zhang, Z., Wu, X.: Indenter geometrical effects on sub-micro/nano indentation and scratch behaviors of polymeric surfaces. Mech. Adv. Mater. Struct. **23**, 291–300 (2016). doi:10.1080/15376494.2014.955154

Willis, J.R.: Hertzian contact of anisotropic bodies. J. Mech. Phys. Solids. **14**, 163–176 (1966). doi:10.1016/0022-5096(66)90036-6

Wu, X., Moon, R.J., Martini, A.: Crystalline cellulose elastic modulus predicted by atomistic models of uniform deformation and nanoscale indentation. Cellulose. **20**, 43–55 (2013). doi:10.1007/s10570-012-9823-0

Xia, W., Song, J., Hsu, D.D., Keten, S.: Understanding the interfacial mechanical response of nanoscale polymer thin films via nanoindentation. Macromolecules. **49**, 3810–3817 (2016). doi:10.1021/acs.macromol.6b00121

Xu, Z., Buehler, M.J.: Interface structure and mechanics between graphene and metal substrates: a first-principles study. J. Phys. Condens. Matter. **22**, 485301 (2010). doi:10.1088/0953-8984/22/48/485301

Xu, M., Tabarraei, A., Paci, J., Oswald, J., Belytschko, T.: A coupled quantum/continuum mechanics study of graphene fracture. Int. J. Fract. **173**, 163–173 (2012). doi:10.1007/s10704-011-9675-x

Yan, W., Pun, C.L., Simon, G.P.: Conditions of applying Oliver–Pharr method to the nanoindentation of particles in composites. Compos. Sci. Technol. **72**, 1147–1152 (2012). doi:10.1016/j.compscitech.2012.03.019

Zandiatashbar, A., Lee, G.-H., An, S.J., Lee, S., Mathew, N., Terrones, M., Hayashi, T., Picu, C.R., Hone, J., Koratkar, N.: Effect of defects on the intrinsic strength and stiffness of graphene. Nat. Commun. **5**, 3186 (2014). doi:10.1038/ncomms4186

Zhang, Y.Y., Gu, Y.T.: Mechanical properties of graphene: Effects of layer number, temperature and isotope. Comput. Mater. Sci. **71**, 197–200 (2013). doi:10.1016/j.commatsci.2013.01.032

Zhang, B., Mei, L., Xiao, H.: Nanofracture in graphene under complex mechanical stresses. Appl. Phys. Lett. **101**, 121915 (2012). doi:10.1063/1.4754115

Zhao, H., Aluru, N.R.: Temperature and strain-rate dependent fracture strength of graphene. J. Appl. Phys. **108**, 64321 (2010). doi:10.1063/1.3488620

http://www.springer.com/978-3-319-52793-2

Micromechanics and Nanomechanics of Composite Solids

Meguid, S.A.; Weng, G.J. (Eds.)
2018, XIII, 519 p. 186 illus., 136 illus. in color.,
Hardcover
ISBN: 978-3-319-52793-2